

# TOWARDS QUANTITATIVE CAVITATION MAPPING FOR TRANSCRANIAL ULTRASOUND HOLOGRAPHIC THERAPY

Nathalie Lamothe <sup>1</sup>, Noé Jiménez <sup>1</sup>, Diego Miguez <sup>1</sup>, Alejandro Cebrecos <sup>1</sup>, Francisco Camarena <sup>1</sup>

<sup>1</sup> Instituto de Instrumentación para Imagen Molecular (I3M), CSIC - Universitat Politècnica de València, Spain  
e-mail: [nojigon@upv.es](mailto:nojigon@upv.es)

## Resumen

El mapeado de la cavitación ha surgido como una herramienta fiable para monitorizar en tiempo real terapias no térmicas de ultrasonidos focalizados basadas en la cavitación de microburbujas. Sin embargo, en aplicaciones de ultrasonido focalizado transcraneal como la apertura de la barrera hematoencefálica, la presencia del cráneo introduce aberraciones que distorsionan los mapas de cavitación. En este trabajo, presentamos un enfoque basado en modelos para la elaboración de mapas de cavitación transcraneal que se utilizará como herramienta de supervisión durante las aplicaciones terapéuticas. Utilizando índices de cavitación correspondientes a la emisión subarmónica, ultraarmónica y de banda ancha obtenemos imágenes cuantitativas de los haces terapéuticos. Esta información se utiliza para vigilar la ubicación del punto focal de los haces de ultrasonidos focalizados mediante hologramas acústicos y para evaluar sus capacidades de cobertura volumétrica, mientras que los índices cuantitativos recuperados se utilizan para el control de la potencia del sistema mediante un bucle de retroalimentación. Los resultados muestran que el mapeado cuantitativo de la cavitación puede aplicarse a la terapia de ultrasonido enfocado transcraneal en tiempo real basada en hologramas acústicos.

**Palabras clave:** Mapeado de cavitación; Ultrasonidos terapéuticos; Microburbujas.

## Abstract

Cavitation mapping has emerged as a reliable tool to monitor non-thermal focused ultrasound therapies based on cavitating microbubbles in real time. However, in transcranial focused ultrasound applications such as blood-brain barrier opening, the presence of the skull introduces aberrations which distort the cavitation maps. In this work, a model-based approach is presented for transcranial cavitation mapping to be used as a monitoring tool during therapeutic applications. Quantitative images of the therapeutic beams are obtained by using cavitation indexes corresponding to sub-harmonic, ultra-harmonic and broadband emission. This information is used to monitor the location of the focal spot of focused ultrasound beams based on acoustic holograms and to evaluate their volumetric focusing performance, whilst the retrieved quantitative indexes are used to control the power of the system by a feedback loop. Results show that quantitative cavitation mapping can be applied to real-time monitoring of transcranial focused ultrasound therapy based on acoustic holograms.

**Keywords:** Cavitation mapping; Therapeutic Ultrasound; Microbubbles.

**PACS nº.** 43.80.Sh, 43.60.Sx

## 1 Introduction

Focused ultrasound in conjunction with microbubbles has become a key therapeutic modality for the non-invasive and non-ionizing treatment of neurological diseases such as Parkinson's or Alzheimer's [1]. This technique allows for the first time to induce the opening of the blood-brain barrier (BBB) in a local and reversible manner and thus facilitate targeted drug delivery [2]. This technology has stimulated the interest of researchers in the development of image-guided FUS systems such as Magnetic resonance image-guided phased array systems (MRIgUS) which is a gold standard mainly used for tissue ablation [3]. These latter systems employ a focused set of piezoelectric transducers to generate a focused beam around their geometric focus and by individually controlling the phase of each transducer, the beam can be directed, and aberrations due to the presence of the skull mitigated. Their use in combination with modern medical imaging for therapy guidance allows precise targeting, online monitoring, and post-treatment evaluation of the ultrasound-mediated bioeffects [4]. However, these systems present limitations when focusing away from the geometric centre and, together with their high cost, lack of portability and long treatment times, limit the enthusiasm of their use for BBB opening.

In contrast, drug-delivery applications via BBB opening usually do not require such a high power as no thermal effects are desired but mainly the mechanical bioeffects of ultrasound-stimulated microbubble activity (*i.e.* acoustic cavitation). Alternative approaches range from inserting a small ultrasound transducer inside the brain [5], but these implants are invasive and can lead to infections; to the use of single element transducers with optical neuro-navigation systems [6], although single element devices cannot compensate for the strong phase aberrations produced by skull refraction and attenuation. More recent studies have also demonstrated that the use of acoustic holograms possess the ability to focus beams through aberrant layers using passive lenses based on metamaterials [7] or phase plates [8].

Even when ultrasound focusing can be efficiently achieved using holograms, the problem of monitoring the treatment is still an open issue. Since one of the most robust indicators of the opening of the BBB is the acoustic emission produced by the cavitation of microbubbles [9], [10], spectral algorithms have been developed for the detection of sub-harmonic and ultra-harmonics generated by cavitation activity [11], [12]. Quantitative and reproducible indexes can be calculated to evaluate the cavitation dose [13], [14], and be used to implement acoustic feedback systems to dynamically control the power delivery system and limit in real time the dose delivered [15][16]. Finally, in soft tissue it is common to beamform cavitation signals to map cavitation activity [17]–[21], however visualizing cavitation activity inside the brain, (*i.e.*, when waves propagate through aberrating media) becomes a challenging problem that has only recently been tackled using MRI [20] and, whilst several attempts have been reported using ultrasound imaging [3], [22]–[25], no robust solution has been proposed yet using ultrasound guided systems.

In this work, we implement a numerical model for passive cavitation imaging. For this first approach, the model is simplified: we do not consider aberrations of the skull and we consider a 2D-problem with axial and lateral dimensions of the transducers. The model is based on a dual transducer experimental setup and the dynamics of the microbubbles, when excited by the focused beam, is described following the Church's viscoelastic model. The goal is to simulate the cavitation of microbubbles located in the surrounding fluid, and more precisely in the theoretical focal zone of the FUS transducer, and to monitor the location of the focal spot by using DAS beamforming imaging method.

## 2 Methods

This study is based on a dual transducer setup, one device is used for therapy and a second probe is used for passive cavitation imaging, paired as shown in Figure 1. A 4-element 0.8-MHz phased array focused

ultrasound (FUS) transducer is used as therapeutic emitter. The FUS transducer has an aperture of 64 mm, a radius of 64 mm and a geometric focal distance of 52 mm. A secondary 64-element 5-MHz phased array transducer was used for imaging and was located confocally. The imaging probe presents a linear arrangement of piezoelectric elements and a pitch of 0.15 mm. The central hole of the FUS transducer allows the introduction of the phased array to align the exit planes of both transducers.

In this theoretical study, we consider blood as surrounding fluid and we set a random distribution of microbubbles located around the focal zone. The emitted signal consists of a short sinusoidal pulse burst with an amplitude of 2 kPa, leading to a peak pressure at the focal spot of 0.5 MPa, as typically used for BBB opening applications [23].

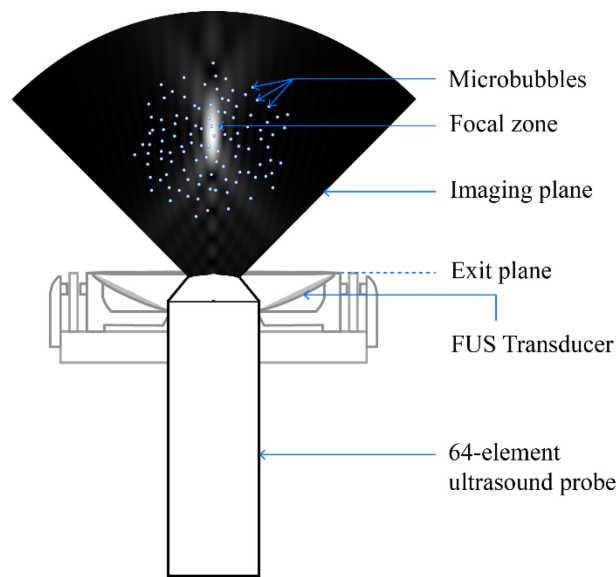


Figure 1 - Experimental setup used for the cavitation mapping study.

## 2.1 Acoustic field calculation

We start calculating the acoustic field produced by the FUS transducer at the locations of the microbubbles. The acoustic field at a point  $\mathbf{r} = \mathbf{r}(x, y, z)$  produced by a vibrating surface located at  $\mathbf{r}_0 = \mathbf{r}_0(x, y, z = 0)$  can be approximated by the Rayleigh-Sommerfeld integral as

$$p(\mathbf{r}) = -i \frac{k}{2\pi\rho_0c_0} \int_{S_0} \frac{v_0(\mathbf{r}_0) \exp(ik|\mathbf{r} - \mathbf{r}_0|)}{|\mathbf{r} - \mathbf{r}_0|} dS_0, \quad (1)$$

where  $v_0(\mathbf{r}_0)$  is the particle velocity normal to the surface  $S_0$ ,  $\rho_0$  the fluid density, and  $k = \omega/c_0$  is the wavenumber at an angular frequency  $\omega$ , and  $c_0$  is the sound speed. From this calculation, the acoustic field is simulated and represented in the Figure 2 where the  $z$ -axis corresponds to the axial direction of the transducer and the  $x$ -axis to the lateral direction.

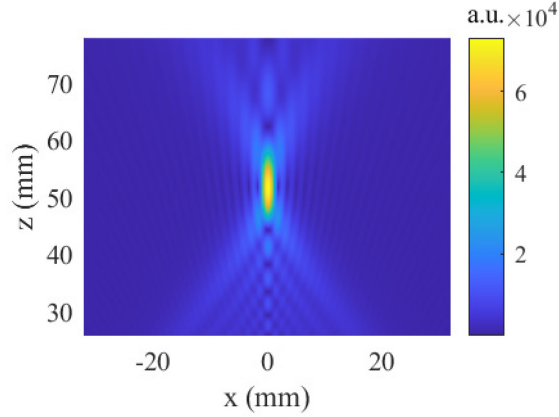


Figure 2 - Acoustic field radiated by a FUS transducer of 0.8 MHz.

## 2.2 Bubble dynamics

Once the impinging ultrasound field amplitude and phase is known on each bubble, we model the vibration of each bubble assuming they do not interact. A Rayleigh-Plesset equation [26] modified to include radiation damping is chosen, as this gives realistic physics while being computationally simple and stable. The shell is described using Church's viscoelastic model, with the exponential stress-strain relationship proposed by Angelsen et al. Shell material parameters are estimated using the methods by de Jong et al. and Hoff et al. [27].

In the limit of small shell thickness in comparison with the radius, the dynamics of an encapsulated gas microbubble follow the equation

$$\rho_l \left( R \frac{\partial^2 R}{\partial t^2} + \frac{3}{2} \frac{\partial R^2}{\partial t} \right) = P_0 \left( \left( \frac{R_0}{R} \right)^{3\gamma} - 1 \right) - P(t) - 4\mu_l \frac{\partial^2 R}{\partial t^2} - 12\mu_s \frac{d_s R_0^2}{R^4} \frac{\partial R}{\partial t} - 12G_s \frac{d_s R_0^2}{R^3} \left( 1 - \frac{R_0}{R} \right), \quad (2)$$

where  $R$  is the bubble radius,  $R_0$  is the bubble radius at rest,  $t$  is the time,  $P_0$  is the ambient pressure,  $P(t)$  is the applied pressure by the ultrasound beam,  $\rho_l$  and  $\mu_l$  are the density and viscosity of the surrounding fluid, e.g., blood,  $\gamma$  is the polytropic exponent of the gas,  $d_s$  is the shell thickness,  $G_s$  is the shear modulus and  $\mu_s$  is the shear viscosity of the shell. Note that the shear modulus and viscosity of the shell are generally frequency dependent, but in this model, it is assumed that they are constant for ultrasonic frequencies. For this study, we use the parameters of SonoVue UCA [28].

## 2.3 Scattered signal

Knowing the variation of the radius with time we can calculate the scattered pressure of the  $m$ -th bubble,  $p_s(t)$ , at a short distance  $r_0$  using the relation

$$p_s(t) = \frac{\rho_l R}{r_0} \left( R \frac{\partial^2 R}{\partial t^2} + 2 \frac{\partial R^2}{\partial t} \right). \quad (3)$$

Note that the waveform of the scattered signal is driven by  $R(t)$  and the distance only contributes to the magnitude of the signal. Therefore, we calculate the scattered signals at a distance  $r = R_0$  and, then, we propagate these signals to each of the elements of the phased array by delaying the scattered waveforms by the corresponding time-of-flight and applying a spherical divergence factor. Therefore, for the  $n$ -th element of the phased array, and for the  $m$ -th bubble, we obtain

$$p_{rf}(n, t) = \sum_m \frac{r_0}{|\mathbf{r}_m - \mathbf{r}_n|} p_s \left( m, t - \frac{|\mathbf{r}_m - \mathbf{r}_n|}{c_0} - t_0(m) \right), \quad (4)$$

where  $\mathbf{r}_n$  is the location of the  $n$ -th element of the phased array and  $\mathbf{r}_m$  is the location of the  $m$ -th bubble, and  $t_0$  is the time of flight of the therapeutic wave travelling from the FUS source to each bubble, which is given by

$$t_0(m) = \frac{|\mathbf{r}_m - \mathbf{r}_0|}{c_0}, \quad (5)$$

where  $\mathbf{r}_0$  is the location of the FUS source, which in this work matches the origin. In this way, the received signal obtained theoretically contains similar information as the received radio frequency (RF) data obtained experimentally.

## 2.4 Cavitation indexes

The behaviour of the microbubble in response to the ultrasound excitation is highly nonlinear and, therefore, we can define several indexes to characterize the dynamic regime. In first place, we can define the harmonic emission as the components of the wave corresponding to integer harmonics of the fundamental FUS frequency. This signal is associated with stable cavitation. Second, we can filter RF data to include only the odd integers of the sub-harmonic component. This signal is associated with inertial cavitation. Third, we can notch filtering RF data to only obtain the sub-harmonic component also associated with inertial cavitation. Finally, we can set a filter bank to extract only the resulting broadband noise after filtering all previous components. This signal is associated with strong inertial cavitation.

## 2.5 Delay and sum beamforming

Once signals have been filtered, image conformation is used for each of the RF data set. For passive cavitation imaging we apply Delay And Sum (DAS) beamforming on an image defined at points in space  $x, z$ . The received signal is then beamformed by time delaying the signal and summing up the contribution of each element. For a frame  $k$ , the beamformed signal is defined as

$$S_k(x, z) = \sum_n p_{rf}(n, \tau(n, x, z)), \quad (6)$$

where the time delay  $\tau(n, x, z)$  is given by

$$\tau(n, x, z) = t_1(x, z) + t_2(n, x, z), \quad (7)$$

and where  $t_1(x, z)$  is the time of flight from the FUS source to the imaging point, given by

$$t_1(n, x, z) = \frac{z \cos \alpha + x \sin \alpha}{c_0}, \quad (8)$$

where  $\alpha$  is the angle between the FUS source and the imaging array, and  $t_2(n, x, z)$  is the time of flight from the imaging location to the  $n$ -th element of the array as

$$t_2(n, x, z) = \frac{\sqrt{(x - x_n)^2 + (z - z_n)^2}}{c_0}, \quad (9)$$

where  $x_n$  and  $z_n = 0$  are the cartesian coordinates of the imaging array. Finally, we can accumulate several frames to obtain a power-cavitation image as

$$S_W = \frac{1}{M} \sum_k |S_k|, \quad (10)$$

where  $M$  is the number of accumulated frames. This process is repeated for each filtered RF dataset to obtain a cavitation image corresponding to the ultra-harmonic, sub-harmonic, broadband emission, and harmonic signals. For the sake of simplicity, in this document we will only show cavitation images using ultra-harmonic, sub-harmonic, and unfiltered RF data.

### 3 Results

#### 3.1 Scattered signal

First, we analyse the scattered signal in the simple case of a 1-cycle pulse and with the existence of one single microbubble in the medium. In Figure 2 we show the emitted pulse and the signal scattered by a single microbubble. Figure 2 (a) shows the waveform of the pulse focused by the source, *i.e.*, at the location of the bubble. The duration of the pulse is  $1.25 \mu\text{s}$  and the amplitude is about  $40 \text{ kPa}$  (note that the bubble is located at the focus zone of the FUS source). Figure 2 (b) shows the theoretical scattered signal at the bubble surface. The single cycle pulse is no longer so well defined, the signal spreads in time and the amplitude is much lower than the emitted pulse. Here, for the microbubble used, the peak of the signal reaches  $0.16 \text{ Pa}$ . This numerically calculated scattered signal is the one that will be received by the imaging probe after propagating through the medium.

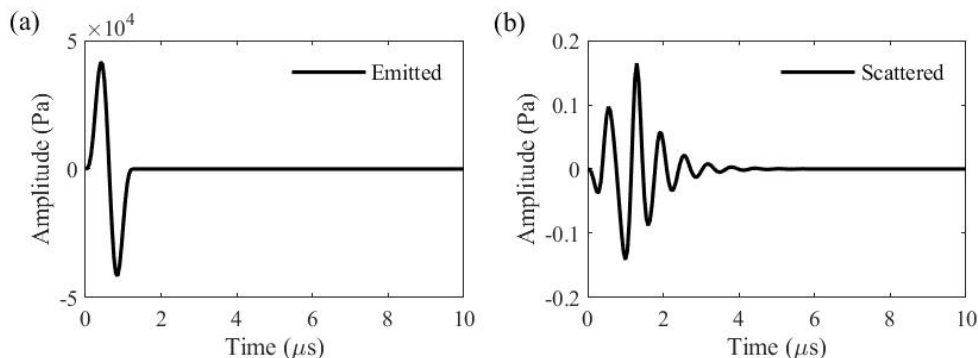


Figure 3 – (a) Emitted signal: 1-cycle pulse at  $2 \text{ kPa}$  and (b) scattered signal at the microbubble surface.

#### 3.2 Beamformed image for a single microbubble

Results of passive cavitation imaging using delay and sum (DAS) beamforming are presented in Figure 3 for one microbubble located in the focal zone of the transducer. The images are arranged in two columns corresponding to two distinct emitted pulses. At the left column we show the results using

$N_c = 1$  cycle for the emitter, being  $N_c$  the number of cycles. At the right column we show the beamformed images using  $N_c = 6$  cycles. For each excitation, the imaging corresponding to three cavitation indexes is plotted. In the Figure 3 (a), the DAS beamforming is processed from the received RF data with no filter. The microbubble is represented by a red dot and the theoretical focus zone by a red ellipse. With an excitation of 1-cycle pulse, we can see a brighter area corresponding to the peak of the scattered signal coming from the microbubble located in the focal spot of the focused ultrasound beam. Here, the axial and lateral resolutions depend on the wavelength of the imaging probe and the duration of the scattered pulse.

Figure 3 (b) shows the same simulation but using a pulse of 6 cycles. As signal spreads in time, constructive interferences during beamforming lead to a decrease in axial resolution, and point spread function widens over a distance of 6 wavelengths of the fundamental frequency of the scattered pulse. In Figure 3 (c), the DAS beamforming is processed from the filtered signal isolating the ultra-harmonics. Here the source zone with maximum amplitude in the centre corresponds to the real position of the scattered pulse whereas the rest of the peaks corresponds to ringing artifacts due to the filter. For the case of a pulse of 6 cycles, Figure 3 (d) shows interferences between the ringing artifacts and the peaks of the pulse cycles but a maximum of amplitude in the focal region of the FUS transducer can still be seen as expected. In Figure 3 (e) and (f), the received signal is filtered before beamforming to map sub-harmonic cavitation. Because of the large wavelength of the sub-harmonic in comparison with the dimension of the imaging probe, the lateral resolution is poor and the artifacts due to the filtering are also present in the axial axis on both sides of the focal point.

### 3.3 Beamformed image for multiple microbubbles

In order to represent a more realistic case with higher concentration of moving microbubbles in the medium, the contribution of multiple microbubbles was calculated following equation (10), which defines a single power cavitation image  $S_W$  by summing up the contribution of various frames. Figure 4 shows the passive cavitation imaging of the focal zone by introducing 200 microbubbles on the numerical model, an emitted signal of 2 kPa and  $N_c = 1$  cycle, and an accumulation of 50 frames. In Figure 4 (a, b), we can identify more precisely the focal zone of the FUS transducer. Due to the high concentration of microbubbles and the accumulation of various images, the ratio between the amplitude of the scattered signal in the focal zone and the residual noise is higher. We can also highlight that despite the presence of microbubbles all around the imaging field, the contribution of the ones located outside the focal zone is negligible regarding to the higher amplitude of scattered signals coming from the bubbles situated in the illuminated region. In Figure 4 (c), the spatial resolution is still relatively low but the focal spot matches roughly with the maximum of amplitude of the FUS transducer.

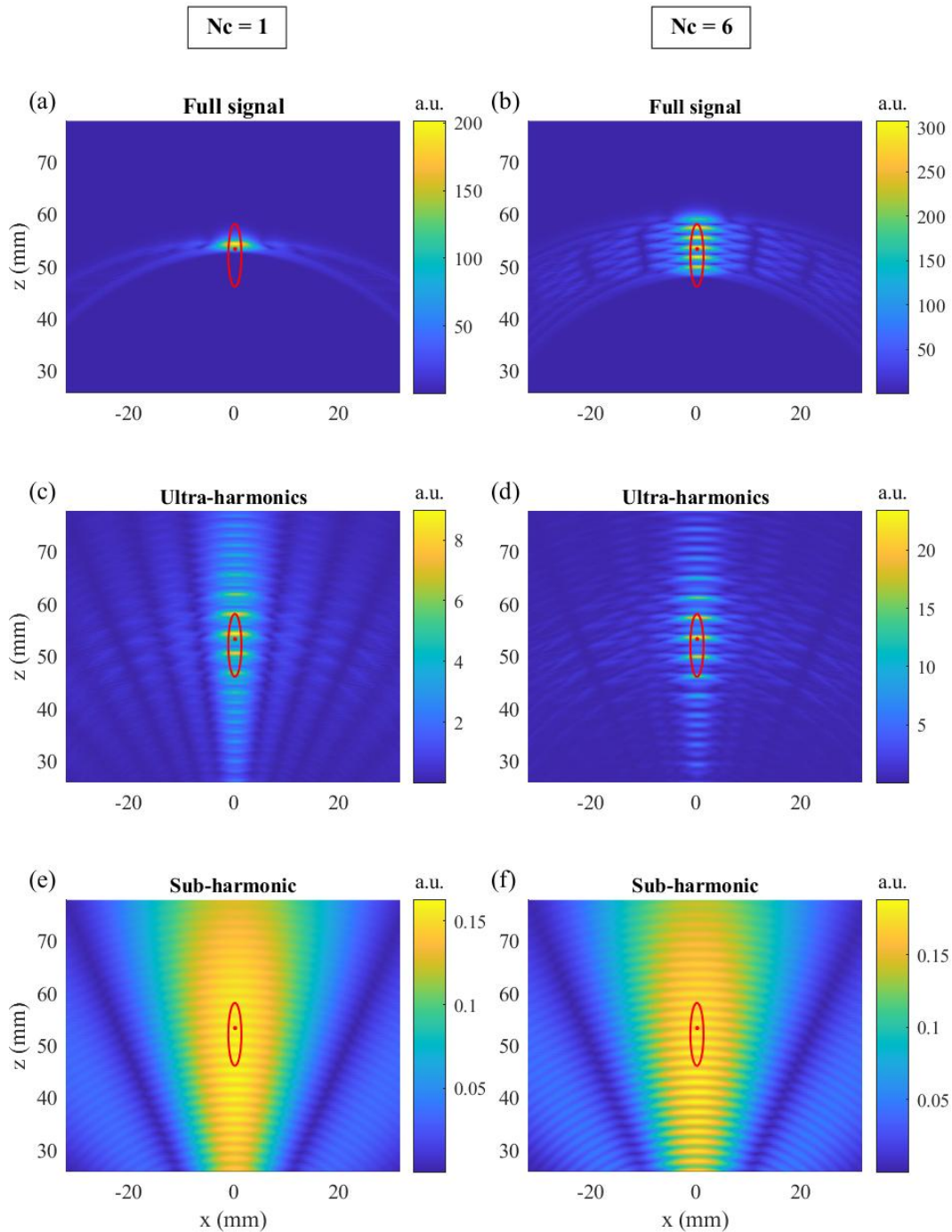


Figure 4 - Passive cavitation imaging using delay and sum (DAS) beamforming for one single microbubble located in the focal zone and for two cases of emitted pulse. Left side: (a) beamforming processed from the received signal with no filter, (c) filtering the received RF signal to map ultra-harmonic cavitation and (e) filtering the received RF signal to map sub-harmonic cavitation, in the case of a pulse of 1 cycle. Right side: (b) beamforming processed from the received signal with no filter, (d) filtering the received RF signal to map ultra-harmonic cavitation and (f) filtering the received RF signal to map sub-harmonic cavitation, in the case of a pulse of 6 cycle.



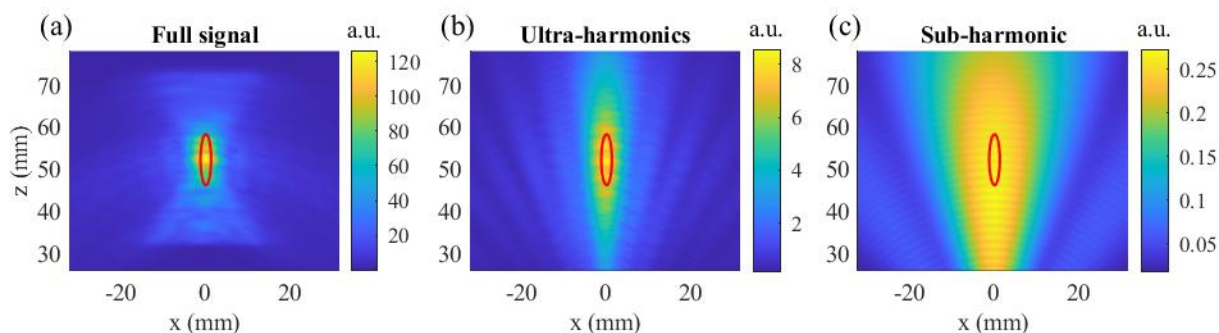


Figure 5 - Passive cavitation imaging using delay and sum (DAS) beamforming for 200 microbubbles located in the imaging field, 50 frames of computation and for an emitted pulse of 1 cycle. (a) Imaging processed from the received signal with no filter, (b) from the filtered signal to map ultra-harmonic cavitation and (c) from the filtered signal to map sub-harmonic cavitation.

## 4 Conclusions

In this work we have presented a theoretical model for the cavitation emission of microbubbles oscillating under the action of a focused ultrasound field. The simulated data was used to obtain beamformed images to map the contribution of ultra-harmonics and sub-harmonic components. Beamformed images show two remarkable features: on the one hand, the brighter areas of the image agree with the focal spot of the focused source. It should be remarked that the goal is not to image the bubbles, but to image only the bubbles cavitating under the action of the therapeutic ultrasound beams. On the other hand, the value of image brightness corresponds to the cavitation index of the filtered data set. Note that the values of the images are weighted by the active duration of the pulse and the duration of the acquisition, and RF data amplitude can be calibrated by using the imaging probe sensitivity. Therefore, by comparing sub-harmonic, ultra-harmonic and harmonic cavitation images one can identify the cavitation regime (inertial or stable) of the bubbles and locate it within the tissue under treatment. Finally, note that sub-harmonic cavitation mapping will suffer only from weak aberrations and absorption by the skull bones during transcranial propagation, offering a robust method for real time monitoring of transcranial focused ultrasound treatments.

## Acknowledgements

This research has been supported by the Spanish Ministry of Science, Innovation and Universities through grant “Juan de la Cierva - Incorporación” (IJC2018-037897-I) and PID2019-111436RB-C22, by the Agència Valenciana de la Innovació through grant INNCON/2020/009. Action co-financed by the European Union through the Programa Operativo del Fondo Europeo de Desarrollo Regional (FEDER) of the Comunitat Valenciana 2014-2020 (IDIFEDER/2018/022).

## References

- [1] N. Lipsman *et al.*, “Blood–brain barrier opening in Alzheimer’s disease using MR-guided focused ultrasound,” *Nat. Commun.*, vol. 9, no. 1, pp. 1–8, Dec. 2018, doi: 10.1038/s41467-018-04529-6.
- [2] H. L. Liu *et al.*, “Blood-brain barrier disruption with focused ultrasound enhances delivery of chemotherapeutic drugs for glioblastoma treatment,” *Radiology*, vol. 255, no. 2, pp. 415–425, May 2010, doi: 10.1148/radiol.10090699.
- [3] M. T. Burgess, I. Apostolakis, and E. E. Konofagou, “Power cavitation-guided blood-brain barrier opening with focused ultrasound and microbubbles,” *Phys. Med. Biol.*, 2018, doi: 10.1088/1361-6560/aab05c.
- [4] K. Hynynen and R. M. Jones, “Image-guided ultrasound phased arrays are a disruptive technology for non-invasive therapy,” *Phys. Med. Biol.*, 2016, doi: 10.1088/0031-9155/61/17/R206.
- [5] C. Horodyckid *et al.*, “Safe long-term repeated disruption of the blood-brain barrier using an implantable ultrasound device: A multiparametric study in a primate model,” *J. Neurosurg.*, vol. 126, no. 4, pp. 1351–1361, 2017, doi: 10.3171/2016.3.JNS151635.
- [6] A. N. Pouliopoulos, S. Y. Wu, M. T. Burgess, M. E. Karakatsani, H. A. S. Kamimura, and E. E. Konofagou, “A Clinical System for Non-invasive Blood–Brain Barrier Opening Using a Neuronavigation-Guided Single-Element Focused Ultrasound Transducer,” *Ultrasound Med. Biol.*, vol. 46, no. 1, pp. 73–89, Jan. 2020, doi: 10.1016/j.ultrasmedbio.2019.09.010.
- [7] C. Shen, J. Xu, N. X. Fang, and Y. Jing, “Anisotropic complementary acoustic metamaterial for canceling out aberrating layers,” *Phys. Rev. X*, vol. 4, no. 4, p. 41033, 2014.
- [8] G. Maimbourg, A. Houdouin, T. Deffieux, M. Tanter, and J.-F. Aubry, “3D-printed adaptive acoustic lens as a disruptive technology for transcranial ultrasound therapy using single-element transducers,” *Phys. Med. Biol.*, vol. 63, no. 2, p. 25026, 2018.
- [9] N. McDannold, N. Vykhodtseva, and K. Hynynen, “Targeted disruption of the blood–brain barrier with focused ultrasound: association with cavitation activity,” *Phys. Med. Biol.*, vol. 51, no. 4, pp. 793–807, Feb. 2006, doi: 10.1088/0031-9155/51/4/003.
- [10] Y.-S. Tung, F. Vlachos, J. A. Feshitan, M. A. Borden, and E. E. Konofagou, “The mechanism of interaction between focused ultrasound and microbubbles in blood-brain barrier opening in mice,” *J. Acoust. Soc. Am.*, 2011, doi: 10.1121/1.3646905.
- [11] C. H. Tsai, J. W. Zhang, Y. Y. Liao, and H. L. Liu, “Real-time monitoring of focused ultrasound blood-brain barrier opening via subharmonic acoustic emission detection: Implementation of confocal dual-frequency piezoelectric transducers,” *Phys. Med. Biol.*, vol. 61, no. 7, pp. 2926–2946, Apr. 2016, doi: 10.1088/0031-9155/61/7/2926.
- [12] C. M. Gorick, N. D. Sheybani, C. T. Curley, and R. J. Price, “Listening in on the Microbubble Crowd: Advanced Acoustic Monitoring for Improved Control of Blood-Brain Barrier Opening with Focused Ultrasound,” *Theranostics*, vol. 8, no. 11, pp. 2988–2991, 2018, doi: 10.7150/thno.26025.
- [13] B. Baseri, J. J. Choi, Y.-S. Tung, and E. E. Konofagou, “Multi-Modality Safety Assessment of Blood-Brain Barrier Opening Using Focused Ultrasound and Definity Microbubbles: A Short-Term Study,” *Ultrasound Med. Biol.*, vol. 36, no. 9, pp. 1445–1459, Sep. 2010, doi: 10.1016/j.ultrasmedbio.2010.06.005.

- [14] S.-M. P. Fletcher, N. Ogrodnik, and M. A. O'Reilly, "Enhanced Detection of Bubble Emissions Through the Intact Spine for Monitoring Ultrasound-Mediated Blood-Spinal Cord Barrier Opening," *IEEE Trans. Biomed. Eng.*, vol. 67, no. 5, pp. 1387–1396, May 2020, doi: 10.1109/TBME.2019.2936972.
- [15] H. A. S. Kamimura *et al.*, "Feedback control of microbubble cavitation for ultrasound-mediated blood–brain barrier disruption in non-human primates under magnetic resonance guidance," *J. Cereb. Blood Flow Metab.*, vol. 39, no. 7, pp. 1191–1203, Jul. 2019, doi: 10.1177/0271678X17753514.
- [16] N. McDannold *et al.*, "Acoustic feedback enables safe and reliable carboplatin delivery across the blood-brain barrier with a clinical focused ultrasound system and improves survival in a rat glioma model," *Theranostics*, vol. 9, no. 21, pp. 6284–6299, 2019, doi: 10.7150/thno.35892.
- [17] M. T. Burgess and E. E. Konofagou, "Fast qualitative two-dimensional mapping of ultrasound fields with acoustic cavitation-enhanced ultrasound imaging," *J. Acoust. Soc. Am.*, 2019, doi: 10.1121/1.5122194.
- [18] P. Kim, J. H. Song, and T. K. Song, "A new frequency domain passive acoustic mapping method using passive Hilbert beamforming to reduce the computational complexity of fast Fourier transform," *Ultrasonics*, 2020, doi: 10.1016/j.ultras.2019.106030.
- [19] M. A. O'Reilly, R. M. Jones, and K. Hynynen, "Transcranial bubble activity mapping for therapy and imaging," *J. Acoust. Soc. Am.*, vol. 134, no. 5, pp. 3975–3975, 2013, doi: 10.1121/1.4830483.
- [20] C. Wu *et al.*, "Monitoring of acoustic cavitation in microbubble-presented focused ultrasound exposure using gradient-echo MRI," *J. Magn. Reson. Imaging*, vol. 51, no. 1, pp. 311–318, Jan. 2020, doi: 10.1002/jmri.26801.
- [21] C. D. Arvanitis, C. Crake, N. McDannold, and G. T. Clement, "Passive Acoustic Mapping with the Angular Spectrum Method," *IEEE Trans. Med. Imaging*, vol. 36, no. 4, pp. 983–993, Apr. 2017, doi: 10.1109/TMI.2016.2643565.
- [22] T. Sun *et al.*, "Closed-loop control of targeted ultrasound drug delivery across the blood–brain/tumor barriers in a rat glioma model," *Proc. Natl. Acad. Sci. U. S. A.*, 2017, doi: 10.1073/pnas.1713328114.
- [23] S. Y. Wu *et al.*, "Transcranial cavitation detection in primates during blood-brain barrier opening—a performance assessment study," *IEEE Trans. Ultrason. Ferroelectr. Freq. Control*, 2014, doi: 10.1109/TUFFC.2014.2992.
- [24] R. M. Jones, L. Deng, K. Leung, D. McMahon, M. A. O'Reilly, and K. Hynynen, "Three-dimensional transcranial microbubble imaging for guiding volumetric ultrasound-mediated blood-brain barrier opening," *Theranostics*, vol. 8, no. 11, pp. 2909–2926, 2018, doi: 10.7150/thno.24911.
- [25] S. Y. Wu *et al.*, "Efficient blood-brain barrier opening in primates with neuronavigation-guided ultrasound and real-time acoustic mapping," *Sci. Rep.*, 2018, doi: 10.1038/s41598-018-25904-9.
- [26] M. S. Plesset and A. Prosperetti, "Bubble Dynamics and Cavitation," *Annu. Rev. Fluid Mech.*, vol. 9, no. 1, pp. 145–185, Jan. 1977, doi: 10.1146/annurev.fl.09.010177.001045.
- [27] L. Hoff and P. C. Sontum, "Acoustic characterization of contrast agents for medical ultrasound imaging," *J. Acoust. Soc. Am.*, 1998, doi: 10.1121/1.422973.
- [28] N. de Jong, L. Hoff, T. Skotland, and N. Bom, "Absorption and scatter of encapsulated gas filled microspheres: Theoretical considerations and some measurements," *Ultrasonics*, 1992, doi:

10.1016/0041-624X(92)90041-J.